MNRAS 000, 1–?? (2018) Preprint 10 July 2018 Compiled using MNRAS LATEX style file v3.0

Stability analysis of core-strahl electron distributions in the solar wind

Konstantinos Horaites,[1⋆] Patrick Astfalk,[2] Stanislav Boldyrev,[1,3] and Frank Jenko[2,4,5]

[1] *Department of Physics, University of Wisconsin – Madison, 1150 University Avenue, Madison, WI 53706, USA*
[2] *Max Planck Institute for Plasma Physics, 85748 Garching, Germany*
[3] *Space Science Institute, Boulder, CO 80301, USA*
[4] *Technical University of Munich, 85748 Garching, Germany*
[5] *The University of Texas at Austin, Austin, TX 78712, USA*

Accepted XXX. Received YYY; in original form ZZZ

ABSTRACT

In this work, we analyze the kinetic stability of a solar wind electron distribution composed of core and strahl subpopulations. The core is modeled by a drifting Maxwellian distribution, while the strahl is modeled by an analytic function recently derived in (Horaites et al. 2018) from the collisional kinetic equation. We perform a numerical linear stability analysis using the LEOPARD solver (Astfalk & Jenko 2017), which allows for arbitrary gyrotropic distribution functions in a magnetized plasma. In contrast with previous reports, we do not find evidence for a whistler instability directly associated with the electron strahl. This may be related to the more realistic shape of the electron strahl distribution function adopted in our work, as compared to previous studies. We however find that for typical solar wind conditions, the core-strahl distribution is unstable to the kinetic Alfvén and magnetosonic modes. The maximum growth rates for these instabilities occur at wavenumbers $kd_i \lesssim 1$ (where d_i is the ion inertial length), at moderately oblique angles of propagation, thus providing a potential source of kinetic-scale turbulence. We therefore suggest that if the whistler modes are invoked to explain anomalous scattering of strahl particles, these modes may appear as a result of nonlinear mode coupling and turbulent cascade originating at scales $kd_i \lesssim 1$.

Key words: solar wind – plasmas – instabilities

1 INTRODUCTION

The low Coulomb collisionality of the solar wind allows electron velocity distribution functions (eVDFs) to persist in a non-thermal state. Solar wind eVDFs exhibit suprathermal populations (e.g., Feldman et al. 1975), in addition to the Maxwellian core, which carry free energy that may drive kinetic instabilities. At 1 AU, suprathermal electrons with energies between ∼10 eV and ∼1 keV are typically divided into two components: the halo and strahl (e.g., Pilipp et al. 1987). The halo component is relatively isotropic, and is often modeled in velocity space as a kappa distribution (e.g., Maksimovic et al. 2005). The strahl, on the other hand, forms a narrow beam in velocity space that is aligned with the local magnetic field **B**, and flows anti-sunward. The strahl component is believed to be composed of "thermal runaway" particles (Gurevich & Istomin 1979), which are seen in collisionless plasmas in the presence of a temperature gradient, that are focused into a beam as they move through a spatially weakening magnetic field (e.g., Scudder & Olbert 1979).

The field-parallel skewness of solar wind eVDFs, and the heat flux associated with it, has spurred the study of so-called "heat flux instabilities" (e.g., Forslund 1970; Gary et al. 1975). In these models, the field-parallel bulk velocity of the core population drifts slightly sunward relative to the ions. This drift offsets the anti-sunward flow of the heat flux-carrying particles so that the net parallel current is nearly zero. If the model parameters are adjusted so that the heat flux and associated core drift amplitude both increase, eventually an instability threshold may be reached for a particular wave mode. Gary et al. (1975) modeled the eVDF as a combination of two drifting Maxwellians, which respectively represented the core and halo populations. They found these core-halo distributions to be unstable to Alfvén,

⋆ E-mail: horaites@wisc.edu

magnetosonic, and whistler mode fluctuations, with instability regimes depending on the wavenumber. Empirically, it has been shown that the electron heat flux q may be constrained by thresholds imposed by the whistler as well as the kinetic Alfvén (Gary et al. 1999; Wilson et al. 2013; Tong et al. 2018) heat flux instabilities; these thresholds are derived assuming a core-halo model eVDF. We note that the core drift and heat flux appear to also be mediated by the Coulomb collisionality of the solar wind, as was shown in large statistical studies of *Wind* satellite data (Bale et al. 2013; Pulupa et al. 2014).

Kinetic instabilities have garnered particular interest in studies of the strahl population, as they may provide a source of scattering of the strahl beam. Such a source was called for by Lemons & Feldman (1983), who incorporated Coulomb collisions into a collisionless model of strahl formation. After comparing with data from the *IMP 8* satellite, it was claimed that pitch-angle scattering by Coulomb collisions alone could not account for the observed angular width of the strahl. Following e.g., Pilipp et al. (1987), we refer to the non-Coulombic scattering that is sometimes invoked to explain the strahl width as "anomalous diffusion" or "anomalous scattering". Recently, Graham et al. (2018) inferred the presence of a strahl-scattering process that occurs over distance, by showing that for 1 AU data measured near SEP events, the angular width of the strahl population is correlated with the length of the interplanetary magnetic field lines that stretch back to the coronal base. Beyond anomalous diffusion, wave-particle scattering of the strahl has been suggested by some authors to be a potential source of the nearly-isotropic halo distribution. For instance, Maksimovic et al. (2005) and Štverák et al. (2009) found that the relative densities of the strahl and halo populations vary inversely with heliocentric distance, providing indirect evidence that the halo population may be formed from scattered strahl particles.

A new analytical model for the strahl distribution was developed in Horaites et al. (2018), by deriving exact solutions to the collisional kinetic equation in the asymptotic high-energy regime relevant to the strahl. This model was fit to eVDF data measured by the *Wind* satellite's SWE strahl detector measured at 1 AU, with remarkable agreement. In particular, it was shown that the model can predict how the angular width of this population scales with particle energy and background density. However, matching this model to 1 AU data also leads to the prediction that the strahl amplitude should *increase* with heliocentric distance—in contradiction with the trend observed by Štverák et al. (2009). The model also predicts, in accordance with Lemons & Feldman (1983), that at a given energy the strahl should become narrower with heliocentric distance—the opposite radial trend that was reported in Hammond et al. (1996); Graham et al. (2017) in the outer heliosphere. Despite the successes of collisional model proposed in Horaites et al. (2018), it may require improvement through the inclusion of additional physical processes.

Examples of such processes are the kinetic instabilities that can be triggered by a non-Maxwellian electron distribution function. In this work we revisit the question of kinetic instabilites in the solar wind plasma, for an eVDF that is composed of parallel-drifting core and strahl components. For the first time we conduct the stability analysis using a realistic distribution function (described above, from Horaites et al. 2018) for the strahl component, derived from the electron kinetic equation. The strahl distribution function is rather nontrivial and, therefore, its stability analysis has to be conducted numerically. For this purpose, we employ the LEOPARD solver (Astfalk & Jenko 2017), which has been recently developed to analyze the stability of arbitrary gyrotropic distributions in a magnetized plasma.

We search for unstable modes that one may expect to be most relevant to a core-strahl eVDF: the Alfvén, magnetosonic, and whistler modes. These modes have been shown to be unstable for model distributions composed of drifting core and halo components. For our core-strahl model, we indeed find that the distributions are unstable to the Alfvén and magnetosonic modes with wavenumbers $kd_i \lesssim 1$. The ion inertial length d_i is defined:

$$d_i = v_A/\Omega_i, \tag{1}$$

where $\Omega_i \equiv eB/m_p$ is the ion cyclotron frequency and v_A is the Alfvén speed. However, we have not been able to identify the whistler modes that would be directly excited by a Cherenkov resonance with the strahl particles; such modes appear to be damped overall. We therefore propose that for the strahl particles to be scattered by the whistler modes (as in, e.g. Vocks et al. 2005; Saito & Gary 2007a), such modes should be generated not by the strahl electrons but rather transferred to small scales as a result of a turbulent cascade, say originating from the core-drift instabilities at $kd_i \lesssim 1$. This result provides a source for whistler waves that is different and complementary to the previously discussed mechanism of whistler instabilities (e.g., Forslund 1970; Gary et al. 1975; Saeed et al. 2017).

The effect of whistler waves on the eVDF has been investigated in Particle-in-Cell (PIC) simulations. For instance, Saito & Gary (2007b) demonstrated that a broadband spectrum of parallel propagating whistlers could significantly broaden the strahl population. We note though that in PIC simulations of whistler turbulence, e.g., Saito et al. (2008) and Chang et al. (2013), the parallel temperature of the eVDF increases with time more quickly than the perpendicular temperature. This calls into question the effectiveness of whistler turbulence as a source of electron pitch-angle (perpendicular) scattering; at least insofar as one might try to explain the presence of the nearly-isotropic halo through direct strahl scattering, as suggested by Štverák et al. (2009). However, these turbulent simulations did not include a strahl component, so the impact of the turbulence on this component has not to our knowledge been directly studied.

We note that our model core-strahl eVDF omits the halo component; this choice is based on practical and theoretical considerations. First of all, halo-driven instabilities are already a well-studied topic that need not be rehashed here, as it is well known for instance that halo temperature anisotropy and core-halo drift can lead to linear instabilities. Furthermore, the inclusion of a halo component would complicate our model by introducing additional free parameters, such as halo anisotropy and relative density, which would needlessly expand the parameter space we wish to explore. We might reasonably try to simplify such a core-halo-strahl model by assuming a strictly isotropic (and monotonic with energy) halo, which would be consistent with the av-

erage properties of this component (Pierrard et al. 2016). But isotropic, monotonic distributions are always linearly stable (e.g., Clemmow & Dougherty 1969), so the inclusion of a tenuous isotropic halo can be expected to have only a slight stabilizing effect, and should not introduce any new instabilities beyond those found with the more straightforward core-strahl model. For empirical support of this claim, see Appendix A, in which we present a preliminary stability analysis of a fiducial core-halo-strahl eVDF.

2 CORE-STRAHL DISTRIBUTION FUNCTION

In order to conduct a stability analysis, we will model the electron velocity distribution function $f(\mu,v)$ as a core-strahl system. Since the distributions are assumed to be gyrotropic, we use as independent variables the velocity magnitude v, and cosine of the pitch angle μ:

$$\mu \equiv \hat{\mathbf{B}}\cdot\mathbf{v}/v, \tag{2}$$

where the unit vector $\hat{\mathbf{B}}$ points along the (Parker spiral) magnetic field, in the anti-sunward orientation.

Let us designate our core and strahl model functions as $f_c(\mu,v)$, $f_s(\mu,v)$, respectively. The total distribution is then $f = f_c + f_s$, and the total density n is given by:

$$\int f(\mathbf{v})d^3v = 2\pi\int_0^\infty\int_{-1}^1 f(\mu,v)v^2 d\mu dv = n. \tag{3}$$

The core Maxwellian distribution $f_c(\mu,v)$ is allowed to drift (sunward) at parallel velocity v_d relative to the protons. This distribution has the form:

$$f_c(\mu,v) = \frac{n_c}{\pi^{3/2}v_{th}^3}\exp\left(\frac{-v^2+2\mu v v_d - v_d^2}{v_{th}^2}\right), \tag{4}$$

where n_c, v_{th} represent the electron core density and thermal speed, respectively.

Our model for the strahl distribution, $f_s(\mu,v)$, comes from Horaites et al. (2018), Eq. (38):

$$f_s(\mu,v) = C_0 A(v)\frac{n_c}{v_{th}^3}\left(\frac{v}{v_{th}}\right)^{2\varepsilon}\exp\left[\tilde{\gamma}\Omega(v/v_{th})^4(1-\mu)\right]. \tag{5}$$

In this expression we use the "effective" Knudsen number introduced in (Horaites et al. 2018, Eq. 26),

$$\tilde{\gamma}(x) = T^2/\left(2\pi e^2\Lambda n_c x\right), \tag{6}$$

where $T(x) = m_e v_{th}^2/2$ is the core electron temperature, Λ is the Coulomb logarithm, and x is the heliospheric distance. We let the parameters ε and Ω be given by empirical measurements (Horaites et al. 2018), representative of the typical ($\tilde{\gamma}=0.75$) fast wind: $\varepsilon \equiv -2.14$, $\Omega \equiv -0.3$. A summary of these constants, that do not vary throughout our analysis, are given in Table 1. The analytic derivation of the strahl shape (5) does not however allow one to obtain the overall strahl amplitude. In (Horaites et al. 2018) the constant C_0 in the strahl distribution was therefore estimated from matching with the observational data. In our current consideration it is kept as a free parameter, and the stability analysis is performed for a range of possible strahl amplitudes C_0.

In Eq. (5) we also introduced a truncation function $A(v)$, to ensure that $f_s \to 0$ as $v \to 0$:

$$A(v) = \frac{1}{1+a(v/v_{th})^b}, \tag{7}$$

$\tilde{\gamma}$	0.75
Ω	-0.3
ε	-2.14
a	10
b	2 ε - 4 = -8.28

Table 1. Constants used in Eq. (5), that are not altered throughout our analysis.

n_c ($\approx n$)	4 cm^{-3}
T	12.21 eV
B	8 nT
C_0	0.234

Table 2. The set of physical constants presented in this table are used as a baseline for our model. These constants are consistent with a $\beta_e = 0.307$, $\tilde{\gamma} = 0.75$ plasma. When we investigate the effect of β_e on stability, a different set of n_c, T, B will be used (see section 3). The strahl amplitude C_0 reported here is a typical value that was measured in the $\tilde{\gamma} = 0.75$ fast wind (Horaites et al. 2018). The parameter C_0 will be varied to investigate its effect on stability, to produce Figs. 1 and 5.

where we defined constants $a \equiv 10$, $b \equiv 2\varepsilon - 4$. The form of this low-energy truncation function is somewhat arbitrary, but its introduction is necessary since Eq. (5) was derived assuming $(v/v_{th})^2 \gg 1$. The function $A(v)$ artificially modifies the strahl only at $v < v_{th}$, where the distribution function is anyway dominated by the core component.

As an input to the kinetic solver, we will assume a steady state where the parallel current $J_\parallel$ is zero. That is, we require:

$$J_\parallel \equiv \int v_\parallel f(\mathbf{v})d^3v = 2\pi\int_0^\infty\int_{-1}^1 f(\mu,v)v^3\mu d\mu dv = 0. \tag{8}$$

We can decompose total parallel current into contributions from the core and strahl, that is:

$$J_\parallel = J_{\parallel,c} + J_{\parallel,s}. \tag{9}$$

The analytic form of the core contribution $J_{\parallel,c}$ follows from Eq. (4):

$$J_{\parallel,c} = n_c v_d, \tag{10}$$

and we can therefore write a simple expression for the core drift v_d that ensures $J_\parallel = 0$:

$$v_d = -J_{\parallel,s}/n_c. \tag{11}$$

Eq. (11) suggests a simple procedure for finding the core drift v_d that ensures $J_\parallel = 0$. First, the strahl distribution $f_s(\mu,v)$ is integrated numerically to find $J_{\parallel,s}$, and this value is substituted into Eq. (11) to find v_d (n_c is given).

In the analysis presented in section 3, we will assume a set of plasma parameters that are representative of the fast wind at 1 AU, that we will use as a baseline. These fiducial plasma parameters—the core density n_c, core temperature T, magnetic field strength B—are presented in table 2. These parameters are consistent with a $\tilde{\gamma} = 0.75$, $\beta_e = 0.307$ plasma, where $\tilde{\gamma}$ is defined in Eq. (6) and the electron beta, β_e, is defined:

$$\beta_e \equiv 8\pi n_c T/B^2. \tag{12}$$

The strahl amplitude C_0, typical of the $\tilde{\gamma} = 0.75$ solar wind (Horaites et al. 2018), is also presented in the table.

3 STABILITY ANALYSIS

We analyze the linear stability of the eVDF using the LEOPARD solver (Astfalk & Jenko 2017), which can calculate the dispersion relation $\omega(\mathbf{k})$ for an arbitrary gyrotropic electron distribution. The imaginary part of our solutions determines the stability of the particular wavemode: stable for $Im(\omega) \leq 0$ and unstable for $Im(\omega) > 0$. We will assume that the large-scale variation in any plasma parameters (density, temperature, E- and B-fields) is slow enough that it can be neglected on the spatial scale of the waves. For simplicity, we assume the background electric field is zero.

The final solution $\omega(\mathbf{k})$ is found through an iterative scheme, that converges most efficiently when the initial guesses for ω, $\mathbf{k}$ are near an actual solution. As a starting point for our analysis, we use fully kinetic dispersion relations of the kinetic Alfvén, fast magnetosonic, and whistler branches in a Maxwellian plasma given in, e.g., Told et al. (2016). By smoothly varying the parameters in our model, we can then scan through different propagation angles and parameter regimes to explore the stability of the branches with respect to our core-strahl distribution.

For each branch, we scanned through the propagation angles $0° < \theta < 89°$, with $1°$ resolution. At these angles, we varied the strahl amplitude across the values $C_0 = 0.000, 0.050, 0.100, 0.200$ while holding $\beta_e = 0.307$ fixed. Holding $C_0 = 0.234$ fixed and scanning through these same angles, we varied beta across the values $\beta_e = 0.307, 0.500, 0.700$. We completed these scans for wavenumbers $0.1 < kd_i < 1.0$ for the magnetosonic mode and $0.1 < kd_i < 4.0$ for the KAW mode. We conducted a similar analysis over the range of wavenumbers $1 < kd_i < 40$ for the whistler mode; however, we investigated only angles $0 < \theta < 79°$ and $\theta = 180°$.

In Fig. 1, we show our numerical results for the kinetic Alfvén (KAW) mode in the range of wavenumbers $0 \lesssim kd_i \lesssim 0.7$. In all figures, frequencies and growth rates are normalized to the ion cyclotron frequency Ω_i and wavenumbers are normalized to the ion inertial length d_i (Eq. 1). We solve for the dispersion relation for different strahl amplitudes C_0 (Eq. 5), represented as different lines in Fig. 1. Note that adjusting C_0 also requires adjustment of the core drift v_d according to Eq. (11). All other physical parameters and constants are as listed in tables 1 and 2. The propagation angle is set to $\theta = 63°$. We see that the distribution becomes unstable if the strahl amplitude is sufficiently large, i.e. in the regime $C_0 \gtrsim 0.20$. We also note that since $Re(\omega < 0)$, the waves propagate with a *sunward* parallel phase speed.

The growth rate of the KAW instability appears particularly sensitive to the propagation angle θ; see Fig. 2. Here we hold the strahl amplitude C_0 constant, and instead vary the propagation angle θ. We see the distribution is only unstable in a range of moderately oblique angles $55° \lesssim \theta \lesssim 69°$, and is maximally unstable at $\theta \approx 63°$.

In Fig. 3, we investigate the KAW instability's dependence on the electron beta. Each line in the figure shows the dispersion relation for a different β_e. The line corresponding with $\beta_e = 0.307$ is generated using the physical parameters given in Table 2. The other lines, representing different β_e, require at least one of the parameters n_c, T, B to be adjusted. Let the fiducial parameters listed in table 2 be written as $n_{c,0}$, T_0, B_0, and let $\beta_{e,0} \equiv 0.307$. To investigate a different plasma beta, $\beta_e = \alpha\beta_{e,0}$ (where $\alpha \neq 1$), we choose n_c, T, B in the following manner:

$$T = \alpha T_0, \tag{13}$$

$$n_c = \alpha^2 n_{c,0}, \tag{14}$$

$$B = \alpha B. \tag{15}$$

This scheme allows us to scale β_e while holding $\tilde{\gamma}$ and the Alfvén speed v_A constant. Holding $\tilde{\gamma}$ constant enables ready comparison with Horaites et al. (2018), while holding v_A constant follows the precedent set by Gary et al. (1994). We see in Fig. 3 that the distribution is unstable in the range $0.2 \lesssim \beta_e \lesssim 0.6$, and is maximally unstable at $\beta_e \approx 0.4$.

The distribution also exhibits a second KAW instability; the unstable regime falls in the range of wavenumbers $1 \lesssim kd_i \lesssim 4$, see figure 4. The unstable waves are more oblique here, with propagation angles falling in the range $78° \lesssim \theta \lesssim 87°$. Although the waves here possess growth rates that are about an order of magnitude larger than the growth rates of the less oblique KAW waves (figure 2), their obliquity makes them less able to couple to whistler waves, and therefore these waves are less relevant to generating whistler turbulence that may scatter the strahl (see section 4).

Our core-strahl model function is also unstable to the magnetosonic mode, as shown in Figs. 5, 6, 7. These plots are analogous to Figs. 1, 2, 3 respectively, but for the magnetosonic mode instead of the KAW mode. In figure 5, we see that the function is unstable for the baseline parameters shown in Table 2. We see in Fig. 5 that for the magnetosonic mode, as with the KAW mode, the distribution is unstable when the strahl amplitude is sufficiently large, i.e. in the regime $C_0 \gtrsim 0.20$. Fig. 6 demonstrates that the largest growth rate occurs at $\theta \approx 60°$, a moderately oblique angle. As with the KAW mode, the instability occurs for $Re(\omega) < 0$; i.e., the

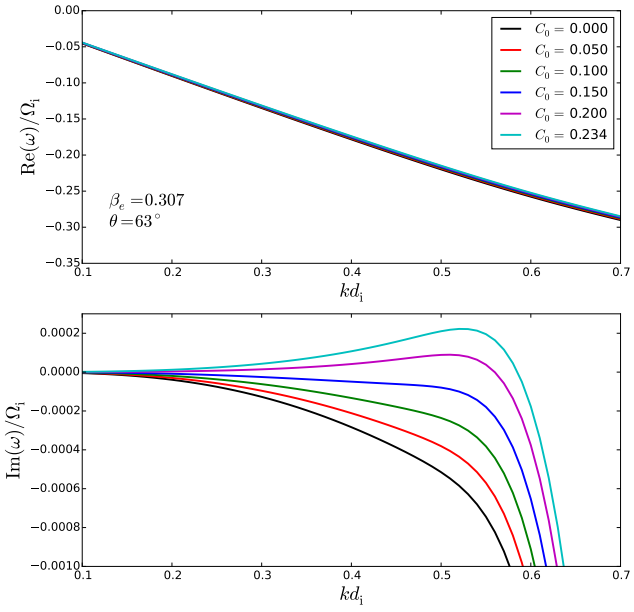

Figure 1. *KAW—Less oblique.* Real (upper) and imaginary (lower) parts of the KAW dispersion relation, shown for different strahl amplitudes C_0. We set $\theta = 63°$ and $\beta_e = 0.307$ for all calculations, but vary the strahl amplitude C_0 (and the core drift v_d, by Eq. (11)). The distribution becomes unstable for $C_0 \gtrsim 0.20$.

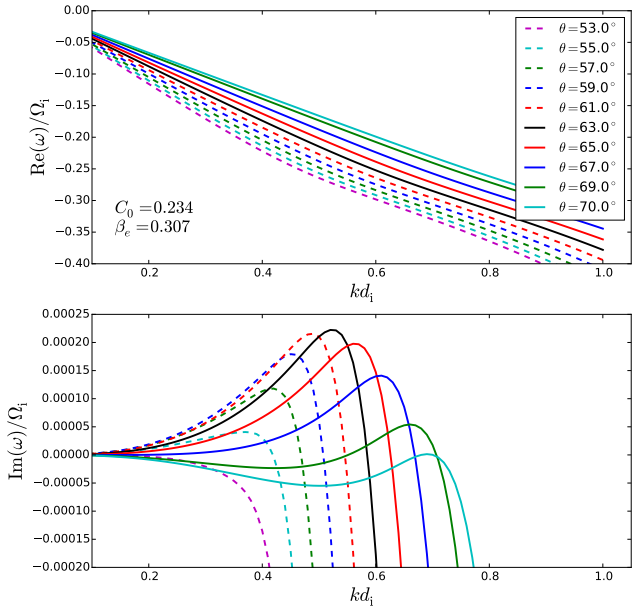

Figure 2. *KAW—Less oblique.* Real (upper) and imaginary (lower) parts of the KAW dispersion relation, shown for different propagation angles θ. We set $\beta_e = 0.307$ and $C_0 = 0.234$ for all calculations, but vary the propagation angle θ. The distribution is unstable in the range $55° \lesssim \theta \lesssim 69°$, and is maximally unstable at $\theta \approx 63°$.

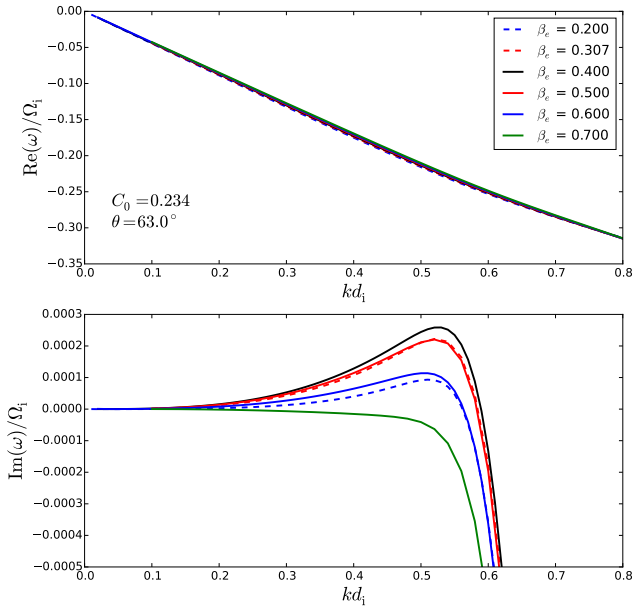

Figure 3. *KAW—Less oblique.* Real (upper) and imaginary (lower) parts of the KAW dispersion relation, shown for different electron betas (β_e). We set $\theta = 63°$ and $C_0 = 0.234$ for all calculations, but vary the electron beta β_e. The distribution is unstable in the range $0.2 \lesssim \beta_e \lesssim 0.6$, and is maximally unstable at $\beta_e \approx 0.4$.

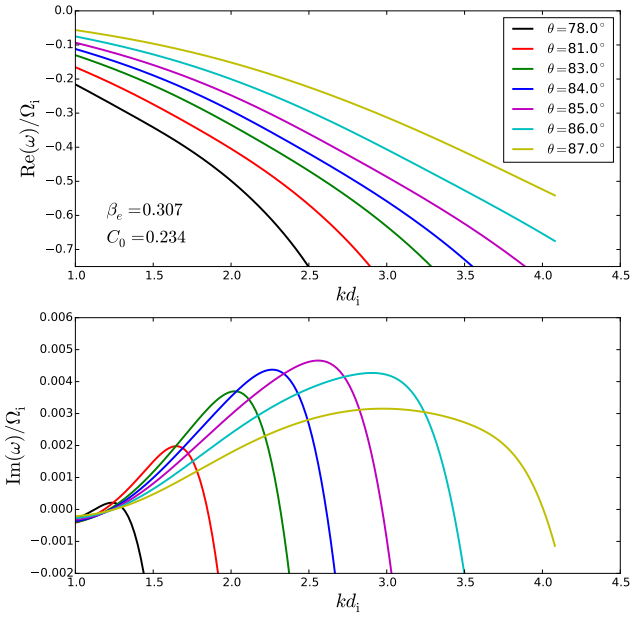

Figure 4. *KAW—More oblique.* Real (upper) and imaginary (lower) parts of the KAW dispersion relation, shown for different propagation angles θ. We set $\beta_e = 0.307$ and $C_0 = 0.234$ for all calculations, but vary the propagation angle θ. Here we see an instability in the range of wavenumbers $1 \lesssim kd_i \lesssim 4$. The distribution is unstable in the range $78° \lesssim \theta \lesssim 87°$, and is maximally unstable at $\theta \approx 85°$.

waves propagate toward the sun. Fig. 7 displays the instability's dependence on β_e; here we see that the distribution is unstable in the range $0.3 \lesssim \beta_e \lesssim 0.7$, with monotonically increasing growth as β_e increases in this range. The parameter β_e was adjusted by varying n_c, T, B in the scheme described by Eqs. (13-15) and the preceding paragraph.

Finally, we note that no instabilities were found for the whistler mode. Although we did observe a whistler mode, all solutions were damped ($Im(\omega) < 0$). In addition to searching through the angles 0°-79°, we checked the stability of antiparallel-propagating ($\theta = 180°$) waves as well. We note that the whistler waves observed recently observed by Stansby et al. (2016), which were attributed to the presence of a heat flux instability, exhibited only parallel and antiparallel propagation angles. For brevity, we do not show a plot of the whistler results, but note only that the absence of a whistler instability is in contrast with the results of Gary et al. (1994), who use a core-halo electron model to show linear theory growth of the whistler heat flux instability.

4 DISCUSSION AND CONCLUSIONS

We here summarize our main results:

1. We analyzed the kinetic stability of a core-strahl eVDF, using a realistic distribution function that is representative of the typical fast solar wind at 1 AU. In agreement with Gary et al. (1975), we observe the eVDF is unstable to the magnetosonic and KAW modes in the range of wavenumbers $kd_i \lesssim 1$. These modes are driven by the Landau resonance with the core electrons, i.e. at parallel velocities

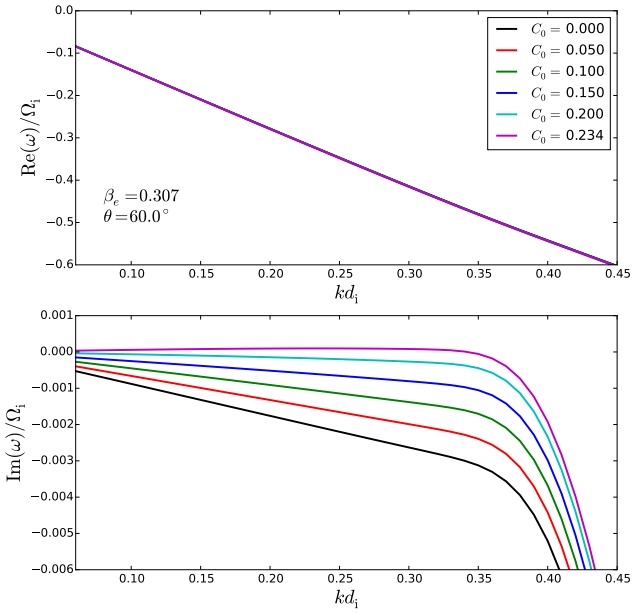

Figure 5. *Magnesotonic.* Real (upper) and imaginary (lower) parts of the magnetosonic dispersion relation, shown for different strahl amplitudes C_0. We set $\theta = 60^\circ$ and $\beta_e = 0.307$ for all calculations, but vary the strahl amplitude C_0 (and the core drift v_d, by Eq. (11)). The distribution becomes unstable for $C_0 \gtrsim 0.20$.

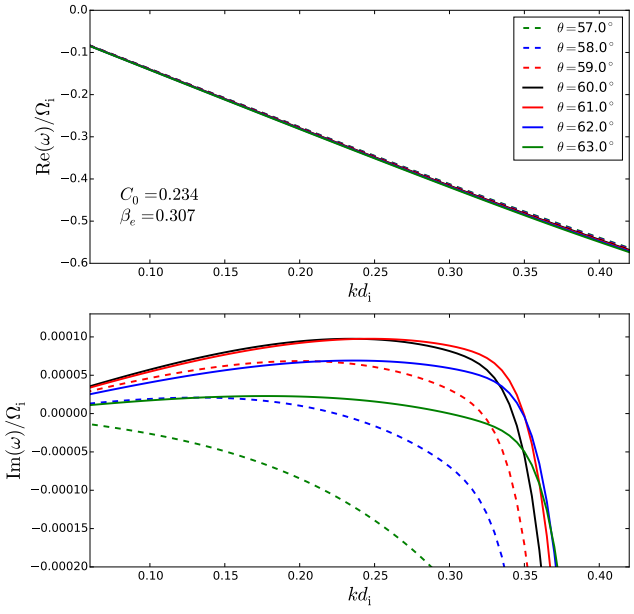

Figure 6. *Magnetosonic.* Real (upper) and imaginary (lower) parts of the magnetosonic dispersion relation, shown for different electron betas (β_e). We set $\beta_e = 0.307$ and $C_0 = 0.234$ for all calculations, but vary the propagation angle θ. The distribution is unstable in the range $58^\circ \lesssim \theta \lesssim 63^\circ$, and is maximally unstable at $\theta \approx 60^\circ$.

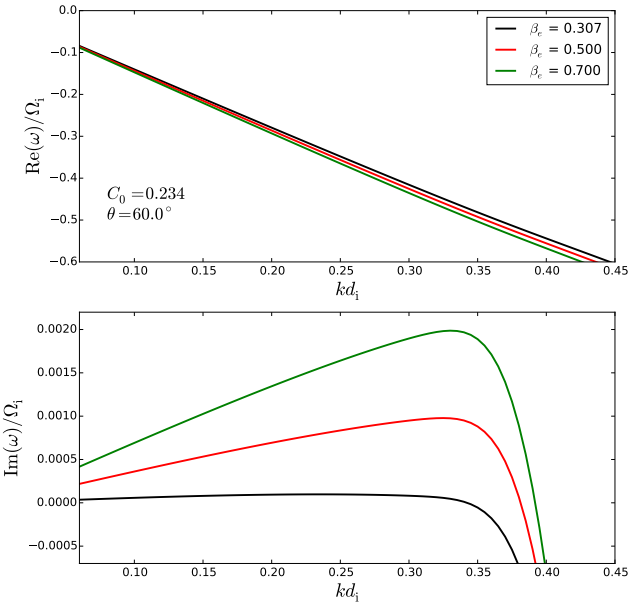

Figure 7. *Magnetosonic.* Real (upper) and imaginary (lower) parts of the magnetosonic dispersion relation, shown for different electron betas β_e. We set $\theta = 60^\circ$ and $C_0 = 0.234$ for all calculations, but vary the electron beta β_e. The distribution is unstable in the range $0.3 \lesssim \beta_e \lesssim 0.7$, with monotonically increasing growth as β_e increases in this range.

$v_\parallel = Re(\omega)/k_\parallel \sim (-v_A)$. The negative sign here indicates that the resonant electrons are traveling slightly sunward, relative to the proton bulk flow. In fact, this resonant velocity falls somewhere between the peaks of the electron and ion VDFs. These results may be fairly insensitive to the particular model used for the core distribution—we note that Forslund (1970) found similar waves and resonances for a core distribution that was non-Maxwellian, i.e. a Maxwellian distorted by a Spitzer-Härm electric field (Spitzer & Härm 1953).

2. Our linear theory analysis does not yield a whistler instability. This begs comparison with the results of Gary et al. (1994), in which a whistler heat flux instability could be excited by a skewed non-thermal eVDF. The difference is likely due to the fact that our model describes a core-strahl rather than a core-halo distribution. That is, the suprathermal heat-flux carrying electrons are modeled by Eq. (5), rather than by a drifting Maxwellian (or other function that is isotropic in its own frame).

The cases where the direct observation of whistler waves has been associated with a large electron heat flux appear to be limited to the slow wind, where the strahl tends to be less prominent (see figures 5 and 9, Lacombe et al. 2014). We propose that further investigation of these events could reveal the presence of a drifting halo; however, to our knowledge such a study has not yet been undertaken.

In the cases where the heat flux is mostly accounted for by the electron strahl, on the other hand, our present work suggests that a large electron heat flux does not necessarily trigger a whistler instability. As a large heat flux is typically associated with a prominent strahl (e.g., Pilipp et al. 1987), caution must be used when parametrizing the stability of

the eVDF in terms of the heat flux, so that the physics of core-halo and core-strahl distributions are not confounded.

3. Remarkably, the observed instability thresholds at $C_0 \sim 0.2$ appear very close to the average strahl amplitude $C_0 = 0.234$ observed in Horaites et al. (2018), for the $\tilde{\gamma} = 0.75$ fast wind. This indicates that the strahl amplitude may be regulated by the instabilities, as has been suggested by other authors. We note that the peak growth rates of the instabilities detected here, with $Im(\omega)/\Omega_i > 10^{-4}$, are just fast enough to be relevant for the solar wind strahl. That is, a typical strahl particle traveling as speed 10^4 km/sec at 1 AU, where the local ion cyclotron frequency is $\Omega_i \sim 1$ Hz, traverses a typical scale height (∼1 AU) in a time $\sim 10^4/\Omega_i$. However, since the observed magnetosonic and KAW modes do not resonate directly with the strahl, we must assume that they could only regulate the strahl amplitude by some indirect mechanism (see also, Tong et al. 2018).

When strong turbulence of moderately oblique kinetic Alfvén and magnetosonic modes is generated at scales $kd_i \lesssim 1$, it can produce whistler fluctuations at the scale $kd_i \sim 1$. These nonlinear fluctuations could then cascade into moderately oblique whistlers at even smaller scales, where they can interact with the strahl electrons, providing their "anomalous" scattering via the cyclotron resonance. This mechanism may also provide an explanation for the moderately oblique whistler-like fluctuations observed in the solar wind by Narita et al. (2016).

APPENDIX A: COMPARISON WITH A CORE-HALO-STRAHL MODEL

In the preceding analysis, we have ignored the halo component, which appears ubiquitously in solar wind eVDFs. Our reasons for omitting this component were described in section 1. In particular, we argued that if we were to assume an isotropic halo, its presence would likely have only a slight stabilizing effect on the distribution. In order to test this claim, we here add a halo component to our model eVDF, and compare the dispersion relations derived from the core-halo-strahl function with those of the foregoing core-strahl model. Rather than conduct an in-depth analysis, we assume some representative halo function with fixed parameters, so as not to introduce any new free parameters to our model.

We will represent the core and strahl distributions by Eqs. 4 and 5, as elsewhere in this paper. Let us then model the halo distribution $f_h(\mu, v)$ as an isotropic kappa function (e.g., Maksimovic et al. 2005; Štverák et al. 2009):

$$f_h(\mu, v) = A_h \left[1 + \frac{m_e v^2}{(2\kappa - 3)T_h}\right]^{(-\kappa-1)}, \quad \text{(A1)}$$

where m_e is the electron mass, and A_h is defined:

$$A_h = n_h \left[\frac{m_e}{\pi(2\kappa - 3)T_h}\right]^{(3/2)} \frac{\Gamma(\kappa+1)}{\Gamma(\kappa-1/2)}, \quad \text{(A2)}$$

where $\Gamma()$ is the gamma function. Table A1 lists our fiducial values for the density n_h, temperature T_h, and kappa parameter κ that appear in Eqs. A1 and A2.

In Figs. A1-A4, we compare the dispersion relations for the core-strahl model (solid lines) with those found for the core-halo-strahl model (dashed lines). In all plots, we see

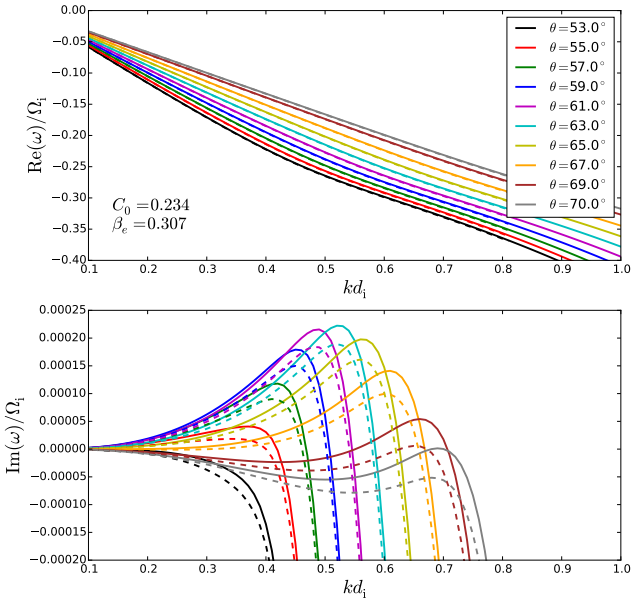

Figure A1. *KAW—Less oblique.* Dispersion relations for the original core-strahl model (solid lines, from Fig. 2) and the core-halo-strahl model (dashed lines) described in this appendix.

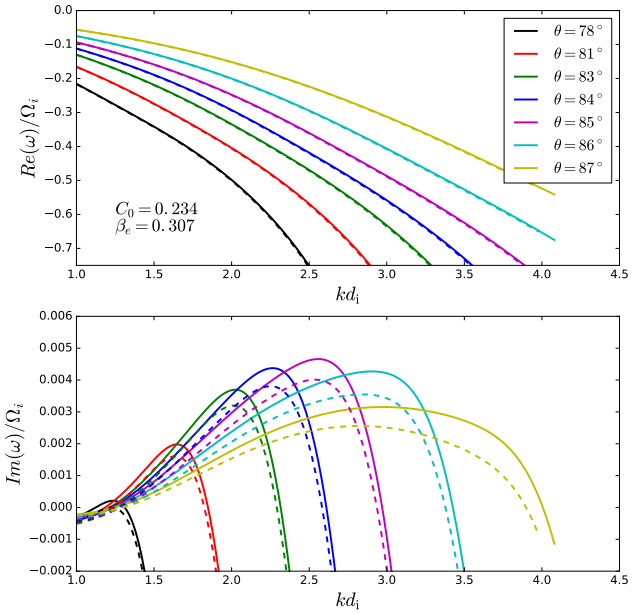

Figure A2. *KAW—More oblique.* Dispersion relations for the original core-strahl model (solid lines, from Fig. 4) and the core-halo-strahl model (dashed lines) described in this appendix.

that $Re(\omega)$ for the wavemodes is not changed significantly, while the $Im(\omega)$ is made slightly more negative due to the damping introduced by the halo.

For the KAW mode, as plotted in Figs. A1, A2, the character of the instabilities are not significantly altered by the inclusion of the halo. Naturally, the extra damping in the core-halo-strahl case slightly narrows the range of angles over which the instability exists.

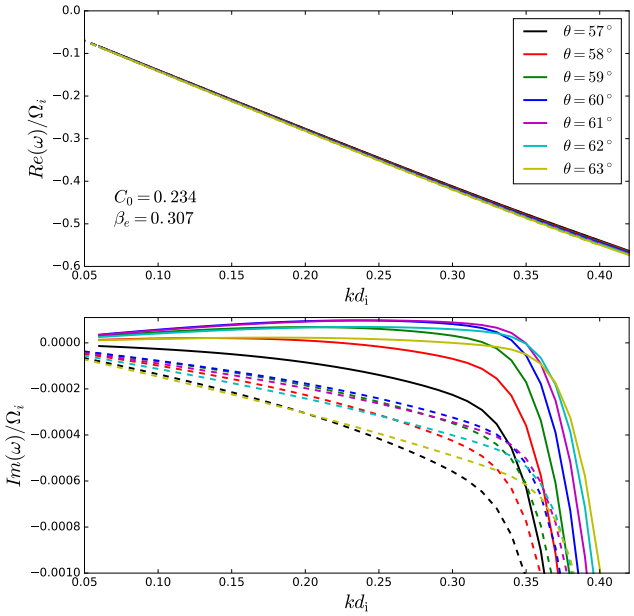

Figure A3. *Magnetosonic.* Dispersion relations for the original core-strahl model (solid lines, from Fig. 6) and the core-halo-strahl model (dashed lines) described in this appendix.

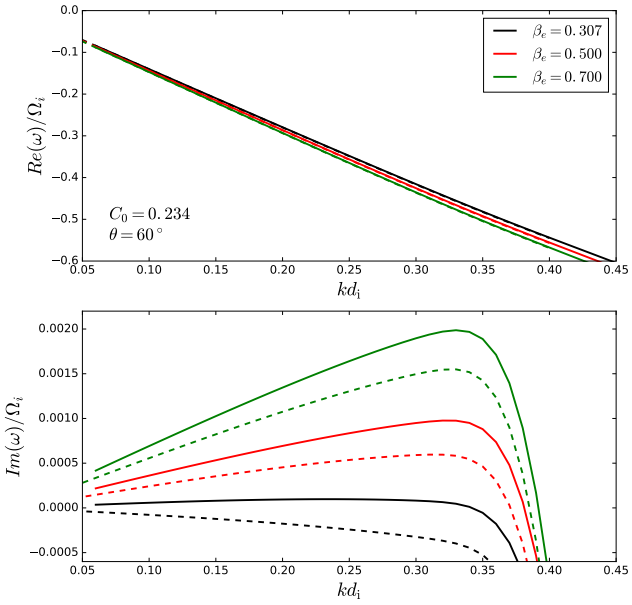

Figure A4. *Magnetosonic.* Dispersion relations for the original core-strahl model (solid lines, from Fig. 7) and the core-halo-strahl model (dashed lines) described in this appendix.

n_h	$n_c/10$
T_h	61.05 eV
κ	5

Table A1. Here we present the set of physical constants, that appear in Eqs. A1 and A2, that specify our halo model.

Inclusion of the halo component has a more noticeable effect on the magnetosonic mode in a $\beta_e = 0.307$ plasma, see Fig. A3. We see that the damping introduced by the halo is significant enough to stabilize this mode at this particular β_e. However, the magnetosonic instability still exists at higher β_e (i.e. at $\beta_e \gtrsim 0.5$), as we can see from Fig. A4. The halo damping thus has the effect of pushing the instability to a slightly different regime in β_e.

As for the core-strahl case, we find that the whistler mode is stable for our core-halo-strahl eVDF.

Acknowledgments—This work of KH and SB was supported by the NSF under the grant no. NSF PHY-1707272 and by NASA under the grant no. NASA 80NSSC18K0646. SB was also supported by the Vilas Associates Award from the University of Wisconsin - Madison.

REFERENCES

Astfalk P., Jenko F., 2017, Journal of Geophysical Research (Space Physics), 122, 89
Bale S. D., Pulupa M., Salem C., Chen C. H. K., Quataert E., 2013, ApJ, 769, L22
Chang O., Gary S. P., Wang J., 2013, Journal of Geophysical Research (Space Physics), 118, 2824
Clemmow P. C., Dougherty J. P., 1969, Electrodynamics of Particles and Plasmas. Addison-Wesley
Feldman W. C., Asbridge J. R., Bame S. J., Montgomery M. D., Gary S. P., 1975, J. Geophys. Res., 80, 4181
Forslund D. W., 1970, J. Geophys. Res., 75, 17
Gary S. P., Feldman W. C., Forslund D. W., Montgomery M. D., 1975, J. Geophys. Res., 80, 4197
Gary S. P., Scime E. E., Phillips J. L., Feldman W. C., 1994, J. Geophys. Res., 99, 23391
Gary S. P., Neagu E., Skoug R. M., Goldstein B. E., 1999, J. Geophys. Res., 104, 19843
Graham G. A., et al., 2017, Journal of Geophysical Research (Space Physics), 122, 3858
Graham G. A., Rae I. J., Owen C. J., Walsh A. P., 2018, ApJ, 855, 40
Gurevich A. V., Istomin Y. N., 1979, Soviet Journal of Experimental and Theoretical Physics, 50, 470
Hammond C. M., Feldman W. C., McComas D. J., Phillips J. L., Forsyth R. J., 1996, A&A, 316, 350
Horaites K., Boldyrev S., Wilson III L. B., Viñas A. F., Merka J., 2018, MNRAS, 474, 115
Lacombe C., Alexandrova O., Matteini L., Santolík O., Cornilleau-Wehrlin N., Mangeney A., de Conchy Y., Maksimovic M., 2014, ApJ, 796, 5
Lemons D. S., Feldman W. C., 1983, J. Geophys. Res., 88, 6881
Maksimovic M., et al., 2005, Journal of Geophysical Research (Space Physics), 110, 9104
Narita Y., et al., 2016, ApJ, 827, L8
Pierrard V., Lazar M., Poedts S., Štverák Š., Maksimovic M., Trávníček P. M., 2016, Sol. Phys., 291, 2165
Pilipp W. G., Muehlhaeuser K.-H., Miggenrieder H., Montgomery M. D., Rosenbauer H., 1987, J. Geophys. Res., 92, 1075
Pulupa M. P., Bale S. D., Salem C., Horaites K., 2014, Journal of Geophysical Research (Space Physics), 119, 647
Saeed S., Sarfraz M., Yoon P. H., Lazar M., Qureshi M. N. S., 2017, MNRAS, 465, 1672
Saito S., Gary S. P., 2007a, Geophys. Res. Lett., 34, L01102
Saito S., Gary S. P., 2007b, Journal of Geophysical Research (Space Physics), 112, A06116
Saito S., Gary S. P., Li H., Narita Y., 2008, Physics of Plasmas, 15, 102305
Scudder J. D., Olbert S., 1979, J. Geophys. Res., 84, 6603

Spitzer L., Härm R., 1953, Physical Review, 89, 977
Stansby D., Horbury T. S., Chen C. H. K., Matteini L., 2016, ApJ, 829, L16
Told D., Cookmeyer J., Muller F., Astfalk P., Jenko F., 2016, New Journal of Physics, 18, 065011
Tong Y., Bale S. D., Salem C., Pulupa M., 2018, preprint, (arXiv:1801.07694)
Vocks C., Salem C., Lin R. P., Mann G., 2005, ApJ, 627, 540
Wilson L. B., et al., 2013, Journal of Geophysical Research (Space Physics), 118, 5
Štverák Š., Maksimovic M., Trávníček P. M., Marsch E., Fazakerley A. N., Scime E. E., 2009, Journal of Geophysical Research (Space Physics), 114, 5104